International Journal of Heat and Mass Transfer 183 (2022) 122167

Contents lists available at ScienceDirect

International Journal of Heat and Mass Transfer

journal homepage: www.elsevier.com/locate/hmt

Reversible sequin fabrics as variable emittance surfaces

Frank Huisman, Eylul Simsek, Tiphaine Galy, Fadi Samaan, Laurent Pilon*

Mechanical and Aerospace Engineering Department, University of California, Los Angeles, Los Angeles, CA 90095-1597, USA

ARTICLE INFO

Article history:
Received 21 April 2021
Revised 13 October 2021
Accepted 19 October 2021

Keywords:
Sequins
Variable emissivity
Spacecraft
Thermal management
Cloaking
Battlefield camouflage

ABSTRACT

This study demonstrates, for the first time, the use of reversible sequin fabrics as inexpensive, scalable, and durable variable emittance surfaces. First, the spectral normal-hemispherical reflectance's of commercially available gold/black and silver/black reversible sequin fabrics were measured at room temperature for wavelength between 0.25 and 20 μm. The surface roughness and material composition of the sequins were also characterized. The dynamic range of the total hemispherical emittance of the gold/black sequin fabric at room temperature was found to be 0.8, exceeding the performance of other variable emittance surfaces reported to date. The use of reversible sequin fabrics for thermal management was demonstrated experimentally by achieving different equilibrium temperatures of the fabric exposed to simulated solar radiation by simply adjusting the sequin pattern. The experimental measurements were in good agreement with a first order transient thermal model. Finally, thermal infrared images were taken of the sequin fabrics to illustrate their capabilities for thermal camouflage, illusion, and messaging.

1. Introduction

Thermal control by variable surface emissivity (or emittance) has been investigated extensively in various engineering applications including spacecraft thermal control [1–3], thermal camouflage [4–6], and thermal management of spacesuits to extend the duration of extra-vehicular activity missions [7].

The Stefan-Boltzmann law expresses the heat transfer rate q (in W) radiated from an opaque surface of surface area A at temperature T (K) as [8]

$$q = \sigma \varepsilon A T^4 \tag{1}$$

where ε is the total hemispherical emittance of the surface while $\sigma = 5.67 \times 10^{-8}$ W/m^2/K^4 is the Stefan-Boltzmann constant. In addition, a surface exposed to solar irradiance G_s in space or in absence of convective heat transfer reaches a steady-state temperature given by [8]

$$T = \left(\frac{\alpha_s}{\varepsilon} \frac{G_s}{\sigma} \right)^{1/4} \tag{2}$$

where changes in the solar absorptance to the emittance ratio α_s/ε determines the range of equilibrium surface temperature achievable.

One way to increase the radiated heat transfer rate is by increasing the surface area A such as in deployable panel radiators for spacecraft thermal management [1,9]. Another way to control the amount of heat dissipated from the surface is to adjust its emissivity. In order to compare variable emittance technologies, the emittance dynamic range $\Delta\varepsilon$ can be defined as [8]

$$\Delta\varepsilon = \varepsilon_{\max} - \varepsilon_{\min} \tag{3}$$

where $\varepsilon_{\max}$ and $\varepsilon_{\min}$ are the maximum and minimum values of the total hemispherical emittance, respectively.

Louvers are the most commonly used device for passive thermal control of spacecraft [10]. They consist of pivoting aluminum blades supported by an aluminum frame mounted on the spacecraft surface. The blades are passively controlled by bimetallic actuator springs that rotate in response to temperature changes. The resulting change in emissivity stemmed from the difference between the emissivity of the aluminum blades and that of the mounting surface, resulting in a typical dynamic range of $\Delta\varepsilon = 0.6$ [10]. Although louvers have extensive space mission heritage, they are rigid, relatively bulky, and very expensive structures [1,10,9]. Therefore, they do not scale well to smaller spacecrafts [1]. In a similar concept of operation, MEMS coatings have been proposed based on electrically actuated microscopic shutters to achieve a theoretical dynamic range of $\Delta\varepsilon = 0.7$, although no experiment was conducted [11]. In general, implementation of MEMS variable emittance surface requires a large power source along with a command and data handling module [3,12,13].

Moreover, Sparrow and Lin [14] found that the apparent spectral hemispherical absorptance of opaque V-groove cavities with specularly or diffusely reflecting surface and under diffuse or collimated irradiation can be varied by adjusting the cavity angle of the V-groove. The authors defined the apparent spectral hemispherical

* Corresponding author.
E-mail address: pilon@seas.ucla.edu (L. Pilon).

https://doi.org/10.1016/j.ijheatmasstransfer.2021.122167
0017-9310/

Nomenclature

A	surface area (m^2)
$B_{nh,\lambda}$	spectral normal-hemispherical reference intensity (%)
C	constant in Eq.(15)
C_{seq}	heat capacity of sequins (J/K)
c_p	specific heat at constant pressure (J/kg/K)
$D_{nh,\lambda}$	spectral normal-hemispherical dark signal (%)
$E_{b,\lambda}$	spectral blackbody radiation emissive power (W/m^3)
g	gravitational acceleration, $g = 9.81$ m/s^2
Gr	Grashof number
G_s	collimated solar radiation (W/m^2)
h	convective heat transfer coefficient ($W/m^2/K$)
k	thermal conductivity (W/m/K)
L	thickness (m)
L_c	characteristic length (m)
$\overline{Nu}_L$	mean Nusselt number
Pr	Prandtl number
q	heat transfer rate (W)
R	surface roughness (nm)
Ra	Rayleigh number
$S_{nh,\lambda}$	measured spectral normal-hemispherical reflected signal
T	absolute temperature (K)
$\bar{T}$	mean temperature (K)
t	time (s)
W	width (m)
x	direction in space

Greek symbols

α	hemispherical absorptance
β	volumetric thermal expansion coefficient (K^{-1})
ε	total hemispherical emittance
ε_n	total normal emittance
ε_λ	spectral hemispherical emissivity
$\Delta\varepsilon$	dynamic range of ε, $\Delta\varepsilon = \varepsilon_{max} - \varepsilon_{min}$
Δt	discretized difference in time (s)
Δx	discretized difference in space (m)
λ	wavelength (μm)
μ	dynamic viscosity (kg/m/s)
σ	Stefan-Boltzmann constant, $\sigma = 5.67 \times 10^{-8}$ $W/m^2/K^4$
ρ	density (kg/m^3)
ρ_A	area density (kg/m^2)
$\rho_{nh,\lambda}$	spectral normal-hemispherical reflectance
$\rho_{std,\lambda}$	standard normal-hemispherical reflectance

Superscripts and subscripts

a	refers to an arithmetic mean roughness
Al	refers to the material aluminum
$cond$	refers to heat transfer by conduction
$conv$	refers to heat transfer by convection
fab	refers to fabric
λ	refers to a spectral property
max, min	refers to maximum and minimum values
nh	refers to a normal-hemispherical measurement
q	refers to a root mean square roughness
rad	refers to radiation
seq	refers to the sequins
std	refers to the high reflecting standard
s	refers to the solar radiation, or of the sun
sur	refers to the surrounding conditions
TC	refers to the thermocouple
∞	refers to the ambient conditions

absorptance as the ratio of the total absorbed energy to the total incoming blackbody radiation. As a fraction of the incident radiation is absorbed by the surface upon each reflection, the apparent absorptance increases when the incident light is reflected within the V-groove a greater number of times. Similarly, the number of reflections increased as the cavity angle decreased. The authors dubbed this "the cavity effect" and developed a graphical model to predict the dynamic range with respect to the cavity angle. For example, a flat diffuse surface with emittance of 0.3 can reach an apparent emittance of 0.7 when featuring V-grooves with a cavity angle of 30°, for a dynamic range of $\Delta\varepsilon = 0.4$ [14].

More recently, Mulford and co-workers [15–18] investigated experimentally the use of origami-inspired tessellated designs for thermal management systems based on the analysis developed by Sparrow and Lin [14]. When deployed, such origami structures transitioned from a folded structure with cavities to a smooth surface. Aluminum shim stock with total hemispherical emissivity of 0.028 at room temperature was used to create these folding structures [15]. For a cavity angle of 14°, the authors found that the apparent emissivity of the origami surface increased to 0.21 for a dynamic range $\Delta\varepsilon$ of 0.182. This dynamic range was in agreement with Sparrow and Lin's model within experimental uncertainty. However, the total amount of energy emitted by a surface depends not only on its apparent emissivity but also on its surface area A, as expressed by Eq. (1). When folding the origami, the apparent emissivity increases but the beneficial cavity effect is reduced by the simultaneously decrease in surface area A. Other variable emittance technologies with different mechanical actuation methods have been investigated. For example, Hu et al. [19] presented a wearable fabric that was able to modulate the amount of IR radiation by more than 35% as strain was applied to the yarn in response to a change in humidity levels.

Moreover, variable emittance technologies based on *electro*chromic and *thermo*chromic materials can achieve a relatively large dynamic ranges, as reviewed by Lang et al. [20]. Electrochromic materials reversibly changed their optical properties through redox reactions occurring when a potential difference is applied across the surface. Demiryont and Moorehead [21] were able to achieve a dynamic range $\Delta\varepsilon = 0.8$ between 7 and 12 μm for a Li-based rigid multilayer electrochromic device operated between ±1 V. Electrochromic devices have also been made from graphene with intercalated ionic liquids [22,23]. Although flexible, these devices were observed to have a dynamic range $\Delta\varepsilon > 0.5$ in the 2.5–45 μm spectral window [6]. Flexible electrochromic devices were also fabricated using polymers such as polyaniline (PANI), polythiophene or poly(aniline-co- diphenyl amine), with dynamic range $\Delta\varepsilon$ on the order of 0.5 in the mid- to far-IR [24,25]. Although it showed fast switching times, the polymer degraded with cycling, and the organic materials became unstable at high temperatures and in presence of UV light. In addition, electrochromic devices need a power system and control modules, adding weight and complexity [20].

Alternatively, the optical properties of thermochromic materials changed as a result of metal-insulator phase transition caused by temperature changes [20]. Two such materials are perovskite manganese oxide MnO_x and vanadium dioxide VO_2. Perovskite MnO_x-based thermochromic devices achieved a maximum dynamic range of 0.43 [20,26,27]. However, the complete phase transition occurred across a large temperature range from −176 to 100 °C [20]. This large temperature range renders it hard to implement for applications that operate at smaller ranges close to room tempera-

ture. The dynamic range achieved by a VO_2–based structure varied from $\Delta\varepsilon = 0.67$ in the 3–5 μm spectral window for VO_2/metal multilayers [28] to $\Delta\varepsilon_\lambda = 0.9$ at wavelength $\lambda = 7$ μm for VO_2 thin films [29]. However, a major drawback of VO_2 is its relatively large transition temperature around 68 °C [28,29]. W-doping can decrease the transition temperature of VO_2 [30]. For example, increasing W-doping from 1 to 2 wt.% reduced the transition temperature from 55 to 35 °C, but it also decreased $\Delta\varepsilon$ from 0.3 to 0.2, measured in the spectral range from 7.5–14 μm [30]. Overall, W-doping can lower the transition temperature of VO_2 but it also reduces the emittance dynamic range [30].

Thermal camouflage, or thermal cloaking, is the process by which dedicated systems are used to hide objects from detection across the thermal radiation spectrum. With the emergence of thermal cameras, concealing objects in the infrared has become part of military tactics. The thermal, or IR camera works by using a microbolometer for every pixel. The microbolometer contains an IR absorbing material that, when exposed to thermal radiation, heats up and changes electric resistance. The resulting resistance is processed as a surface temperature and each pixel is assigned a color. Since emissivity is a measure of a surface's effectiveness in emitting thermal energy, a surface with low emissivity will emit less thermal radiation and will be perceived as cold while a surface at the same temperature but with high emissivity will be perceived as hot. This property is useful in thermal camouflage applications, since the emissivity of the object can be adjusted so that a hot object may be observed as a cold object and vice versa. In addition, if the amount of the radiation intensity emitted by an object matches that of the background, they will have the same perceived temperature and the thermal imager will not be able to distinguish the object from its surroundings. Thermal camouflage systems are usually evaluated by their ability to (i) match varying background temperatures or (ii) conceal hot (or cold) objects as cold (or hot) ones by decreasing (or increasing) their emissivity [20,23].

Many technologies have been used in thermal camouflage applications. Dynamic camouflage is preferred for environments where the background temperature varies. Hu et al. [31] reviewed emerging technologies in this field. Some activation methods include (i) optical (UV) modulation with a maximum dynamic range in emissivity of 0.16; (ii) strain modulation with a dynamic range from 0.5 to 0.81 (at an ambient temperature of 623 K); and (iii) chemical and wetted modulation that can achieve dynamic ranges close to 0.64 [31]. Another way thermal camouflage can be achieved is with the creation of "virtual" heat sources or thermal illusion. Hu et al. [32] experimentally investigated the effect of geometry and location of the virtual heat sources in order to achieve good thermal illusion. Although effective, creating a virtual heat source is often more difficult than controlling dynamically the thermal radiation emitted by a surface.

Finally, Song et al. [33] investigated theoretically the use of metal/insulator/metal (MIM) microstructures to tune the emissivity of a surface pixel-by-pixel using magnetic polaritons at a microscopic scale. For example, a non-uniform temperature distribution on a plate could be perceived by an IR camera as uniform by adjusting the emissivity of each pixel. Such surfaces can also create patterns, images, or messages, leading to thermal illusion and messaging capabilities. Furthermore, Liu et al. [34] experimentally demonstrated thermal camouflage using a metal- liquid-crystal-metal (MLCM) platform. The angle of the crystals in the liquid crystal layer were adjusted to vary the emittance between 0.81 and 0.98. Although this metasurface has a limited range of emittance, it achieved some level of thermal camouflage.

Table 1 summarizes and compares the performance of the different variable emissivity technologies previously discussed. In order to be effective, the thermal management device should feature (1) a large dynamic range near room temperature of $\Delta\varepsilon > 0.7$ [21],

Table 1
Summary of available technologies. The gray highlight shows the maximum dynamic range achieved by any study.

Refs.	Technology	Material	α_s	ε_{min}	ε_{max}	$\Delta\varepsilon$	Wavelength range (μm)	Advantages	Disadvantages
[15]	Origami design	Al. (alloy 1145) in accordion pattern	–	0.028	0.297	0.269	1.5–21	Adaptable and reliable.	Loss in surface area when folded
[21]	Electrochromism	Li-based device (EclipseVED™)	–	–	–	0.7	2–27	Light weight and scalable	Power system and command module
[22]	Electrochromism	Multilayer graphene with intercalated IL	–	0.41	0.57	0.16	–	Flexible	Power system and command module
[23]	Electrochromism	Multilayer graphene with intercalated IL	–	0.33	0.76	0.43	10	Flexible/stretchable, high temp.	Power system and command module
[6]	Electrochromism	Single membrane, 2-electode system	0.29 - 0.50	0.325	0.771	0.446	2.5–45	Flexible, durable and scalable	Power system and command module
[29]	Thermochromism	Phase change in VO_2 thin films	–	0.22	0.71	0.49	2.5–25	No power required	High transition temperature (68 °C)
[28]	Thermochromism	Optimization of multilayer VO_2	–	–	–	0.67	3–5	No power required	High transition temperature (68 °C)
[30]	Thermochromism	W doped VO_2 thin films	–	0.478	0.718	0.240	7.5–15	Lower transition temp. (55 °C)	Reduced dynamic range
[26]	Thermochromism	Phase change in perovskite manganese oxide	0.87	0.19	0.60	0.41	2.5–100	Lower transition temp. (−13 °C)	Reduced dynamic range
[27]	Thermochromism	Phase change in perovskite manganese oxide				0.43	2.5–25	Optimized dynamic range	Large transition temp. range
[10]	Louvres	Pivoting aluminum blade design	–	0.14	0.74	0.60	–	Space mission heritage	Bulky, expensive, not scalable.
[34]	Metasurface	Metal-Liquid-Crystal-Metal based	–	0.81	0.98	0.17	6–20	High resolution	Low tunability
Present study	Sequins	Unknown bulk material	0.38/0.64	0.13	0.85	0.72	2–20	Flexible, scalable, cheap	Activation method

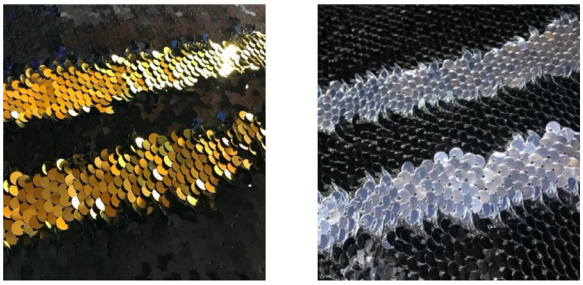

Fig. 1. Photograph of the (a) gold and black and (b) silver and black coated sequin fabrics investigated. Note how a brushing action reveals the gold or silver underside of the sequins by flipping them over.

(2) flexibility as opposed to a rigid structure [6], (3) scalability so it can be applied to large and small structures alike [21], (4) simplicity and durability of the design and compatibility with the environment of its intended use [20]. Each of these properties can be found in some of the technologies previously reviewed, yet none of these technologies meet all these requirements. The reader is referred to Refs. [19,20,31] and references therein for a thorough review of the different types of variable emittance devices and their applications.

Finally, sequin fabrics consist of overlapping parallel rows of sequins tethered by a thread lining the edge of the sequin. This enables the individual sequins to flip in a direction perpendicular to the rows along which they are sewed. In addition, sequins have different coating on each face so that brushing across the sequins results in the fabric taking on different arbitrary appearances and emittances. Such fabric is widely used in fashion and in interior design. However, to the best of our knowledge, it has not been considered as a variable emittance surface for thermal management and camouflage applications. The present study aims to demonstrate the use of reversible sequin fabrics as simple, flexible, scalable, and durable variable emittance surfaces with a large emittance dynamic range to be used in thermal management and thermal camouflage.

2. Materials and methods

2.1. Materials characterization

Black fabrics covered with sewn sequins (David's Accessories) were used as representative of commercially available reversible sequin fabrics. Fig. 1 shows (a) gold and black and (b) silver and black reversible sequin fabrics that were characterized as received. Each sequin was a disk 5 mm in diameter with a 1 mm hole at the top for sewing. The face of the sequins can be reversed by simply brushing a hand over the sequins' surface in the direction opposite to the sequin's alignment.

2.1.1. Surface roughness characterization

The roughness of a surface is known to have a strong effect on its emittance [8]. Thus, individual sequins were cut off the fabric and the root mean square R_q and the arithmetic mean R_a surface roughnesses were measured for each side of the sequins using Atomic Force Microscopy (Veeco Dimension 3000, Digital Instruments Inc.) in tapping mode. The surface roughness of the sequins was measured over a surface area of 15 $\times$ 15 μm^2 at three different locations on both sides of each of the sequins. The average and standard deviation of the roughnesses R_q and R_a were calculated for each side of the sequins from measurements at these three different locations.

2.1.2. Bulk material characterization

To identify the substrate material of the sequins, the coating on individual sequins was first removed. The coatings for the gold sequins were removed by placing them in aqua regia HNO_3 + 3 HCl (Fisher Scientific, USA) until the coating dissolved. The coatings for the silver sequins were removed by performing a stripping reaction using sulfuric acid. Once the coatings were removed, the sequins appeared transparent. For each sequin fabric, several transparent sequins were then hot pressed to obtain a film of thickness around 40 μm, as illustrated in Fig. S1. Then, composition analysis was performed using a nitrogen-purged FTIR spectrometer (Nicolet^{TM} iSTM50, Thermo Scientific) in transmittance mode in the 2.5–20 μm spectral range. The absorption spectra were analyzed and compared to the Hummel Polymer Sample Library included in the Thermo-Fischer OMNIC software. This process was performed on the sequins of both sample fabrics.

2.1.3. Optical properties in the UV and visible range

Before measuring the properties of the sequin fabric, 5 $\times$ 5 cm^2 coupons were cut and wiped clean with a non-abrasive alcohol-free wipe. Then, the normal-hemispherical reflectance $\rho_{\mathrm{nh},\lambda}$ of each face of the two sequin fabrics in the spectral range of 250–1100 nm was measured using a UV–Vis spectrometer (Evolution^{TM} 201 UV-Visible Spectrophotometer, Thermo Scientific) fitted with an integrating sphere accessory (DRA-EV-600, Thermo Scientific). The spectral normal-hemispherical reflectance $\rho_{\mathrm{nh},\lambda}$ was estimated according to [35]

$$\rho_{\mathrm{nh},\lambda} = \frac{\mathrm{S}_{\mathrm{nh},\lambda} - \mathrm{D}_{\mathrm{nh},\lambda}}{\mathrm{B}_{\mathrm{nh},\lambda} - \mathrm{D}_{\mathrm{nh},\lambda}} \rho_{\mathrm{std},\lambda}. \tag{4}$$

Here, the spectral normal-hemispherical reflectance signal $S_{nh,\lambda}$ measured by the FTIR was corrected by subtracting the dark signal $D_{nh,\lambda}$ measured by blocking any light from reaching the detector. The difference $S_{nh,\lambda}$ - $D_{nh,\lambda}$ was normalized by the corrected baseline spectral reflectance measurement $B_{nh,\lambda}$ - $D_{nh,\lambda}$ corresponding to the spectral normal-hemispherical reflectance of a calibrated specular reflection standard mirror (NIST certified STAN-SSH, Ocean Optics) with known standard normal-hemispherical reflectance $\rho_{\mathrm{std},\lambda}$. For each side of both sequin fabrics, the reflectance measurements were repeated at five different spots on the sequin fabric and averaged to account for intra-sample variability in the sequin properties and alignments.

2.1.4. Emittance of the sequin fabrics

First, the spectral normal-hemispherical transmittance and reflectance of samples of the two sequin fabrics (Fig. 1) were measured at wavelength between 1 and 20 μm using the same FTIR spectrometer (Nicolet^{TM} iSTM50, Thermo Scientific) equipped with an integrating sphere (PIKE Technologies, USA). A KBr beamsplitter and a liquid-nitrogen cooled Mercury-Cadmium-Telluride (MCT) detector were used in the spectral range between 2 and 20 μm and a Calcium fluoride (CaF_2) beamsplitter with an InGaAs detector were used in the 1–2.5 μm range. In addition, transmittance measurements were performed on the fabric alone to ensure that it was opaque in the IR. The spectral transmittance for both the sequin fabrics and the fabric alone was found to vanish across the spectral window of 2–20 μm (see Supplementary Material, Figs. S2 and S3) and confirmed that the samples were opaque. Then, according to Kirchhoff's' law, the sequin fabrics' spectral normal emissivity $\varepsilon_{\mathrm{n},\lambda}$ can be expressed as [8,36]

$$\varepsilon_{\mathrm{n},\lambda} = \alpha_{\mathrm{n},\lambda} = 1 - \rho_{\mathrm{nh},\lambda}. \tag{5}$$

Moreover, the total normal emissivity ε_{n} can be calculated from the spectral normal emissivity $\varepsilon_{\mathrm{n},\lambda}$ according to [8,36]

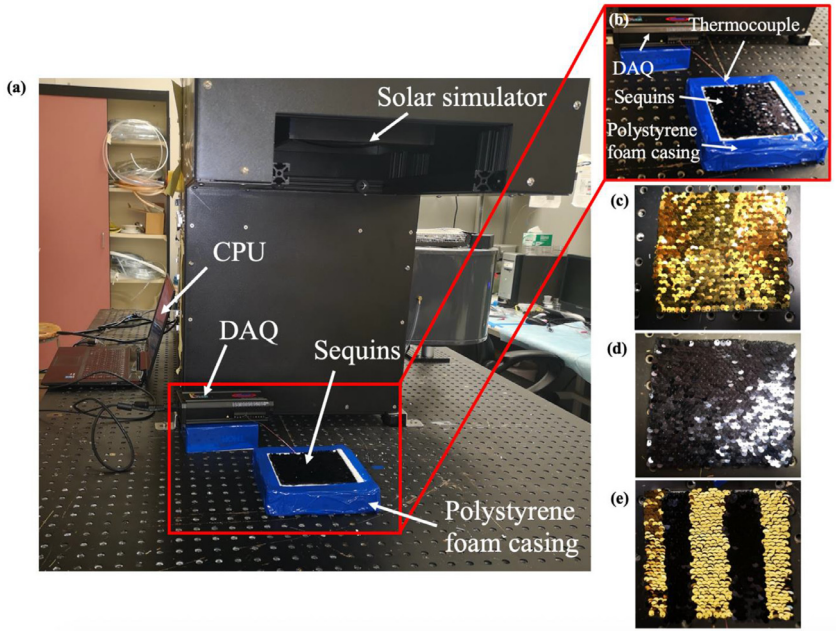

Fig. 2. (a) Photograph of the experimental setup with the solar simulator (TriSol TS-300, OAI, USA), (b) a close-up of the test setup of the black sequins in a polystyrene casing, with the thermocouple and the DAQ module, and (c) the gold, (d) black, and (e) mixed sequin configurations used to test the thermal response under solar irradiation.

$$\varepsilon_n = \frac{\int_0^\infty E_{b,\lambda}(T)\varepsilon_{n,\lambda}\, d\lambda}{\int_0^\infty E_{b,\lambda}(T)\, d\lambda} \tag{6}$$

where $E_{b,\lambda}(T)$ is the spectral Planck's blackbody radiation emissive power at surface temperature T (in K) [8]. Note that the integrals in both the numerator and denominator of Eq. (6) were truncated to the range 2–20 μm while the sample temperature T was 296 K. The lower limit for this truncation results from the fact that the fraction of blackbody radiation at room temperature in the 0–2 μm range is effectively zero and that the sequins are opaque in the 2–20 μm spectral window. This approach was validated for the total normal emissivity of optically smooth surfaces with small (gold and aluminum) and large (fused silica glass) emissivities calculated using Eq. (6) for different integration limits, as summarized in Table S1 in Supplementary Materials.

Finally, although the emittance of all surfaces exhibit some dependence with direction, the total hemispherical emissivity ε typically does not differ greatly from the total normal emissivity ε_n over a wide angular window around the normal direction for dielectric materials [8]. Therefore, the total (or spectral) hemispherical emissivity can be approximated as the total (or spectral) normal emissivity for nonconductors, i.e., $\varepsilon \approx \varepsilon_n$ [8].

The solar absorptance α_s was calculated according to [8]

$$\alpha_S = \frac{\int_0^\infty E_{b,\lambda}(T_S)\varepsilon_{n,\lambda}\, d\lambda}{\int_0^\infty E_{b,\lambda}(T_S)\, d\lambda} \tag{7}$$

where T_S is the temperature of the sun treated as a blackbody at $T_S = 5800$ K [8]. Then, α_S was calculated by truncating the limits of the integrals in Eq. (7) to 0.25-3 μm for both the numerator and the denominator.

2.2. Proof of concept demonstrations

Two experiments were conducted in order to illustrate the applications of sequin fabrics' for thermal management and thermal camouflage. The first experiment aimed to evaluate the use of the variable emittance sequin fabric for thermal management under incident simulated solar radiation. Fig. 2(a) and 2(b) show the experimental setup consisting of (i) surface area $A = 7.6 \times 7.6$ cm^2 sequin fabric attached with thermal paste (AATA-5 G, Arctic Silver) to an aluminum plate of thickness $L_{Al} = 12.7$ mm with the same surface area, (ii) a solar simulator (TriSol TS-300, OAI, USA) providing collimated simulated solar radiation in the wavelength range between 0.4 and 1.1 μm with total radiation flux incident on a surface perpendicular to the collimated simulated radiation of $G_s = 1$ kW/m^2, and (iii) a thermocouple connected to a data acquisition system (Personal DAQ/55, IOTech) and to a computer to record the temperature of the Al plate for different sequin configurations. The Al plate was placed in a custom-made polystyrene casing to ensure proper thermal insulation and leaving the sequins flush with the top surface. A type-T thermocouple (OMEGA, USA) was embedded at depth $L_{TC} = 1.3$ mm below the top surface of the aluminum plate through a hole drilled from the back of the plate and secured with thermal paste. Three types of sequin configurations were tested namely (1) all black, (2) all gold, and (3) a combination of half black and half gold, as illustrated in Fig. 2(c) to 2(e).

The second experiment aimed to illustrate their thermal camouflage capabilities through IR images [5]. Here, an IR camera (E4, FLIR systems, USA) was used to capture IR images of sequin fabric draped over an open acrylic box. Fig. 3 shows images of the experimental setup taken indoors at room temperature (21 °C) and featuring an incandescent lightbulb, acting as a heat source, (a) without the sequin and behind the gold sequin fabric sheets in (b) either black or gold modes, (c) striped mode, and (d) with UCLA letters written in black on the gold sequins.

3. Thermal analysis

3.1. Schematic and assumptions

Fig. 4 shows the schematic of the experimental setup consisted of the sequin fabric in thermal contact with an aluminum plate and embedded in a polystyrene casing along with the associated coordinate system. An energy balance for the sequins at temperature $T_{seq}(t)$ and for the aluminum plate at $T_{Al}(x,t)$ was performed. The sequins absorbed the simulated solar irradiance G_s and lost

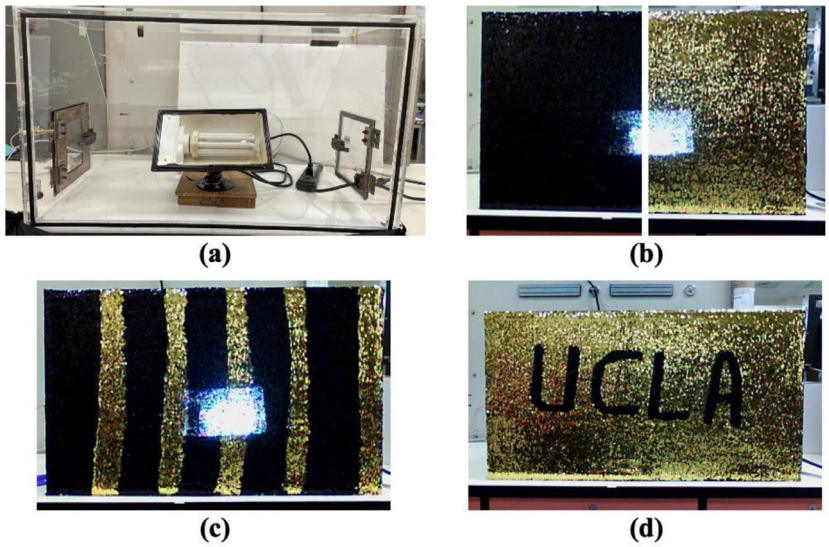

Fig. 3. Photographs of the experimental setup used to demonstrate thermal camouflage, illusion, and messaging. (a) The lightbulb is shown sitting inside an open acrylic box. (b,c,d) box covered by the gold sequin fabric sheet in different configurations in (b) either black or gold modes (lamp on), (c) striped pattern (lamp on), and (d) with UCLA letters written in black on gold (lamp off).

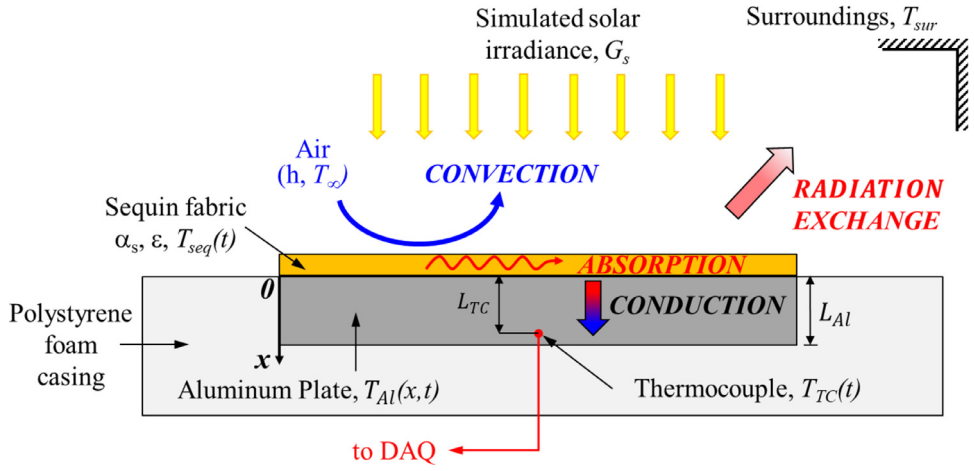

Fig. 4. Schematic of the modeled experimental setup depicting the sequin fabric at $T_{seq}(t)$ exposed to convection and collimated and normally incident simulated solar radiation and in thermal contact with the aluminum plate at $T_{Al}(x,t)$ inside a polystyrene foam casing ensuring thermal insulation. Not to scale.

energy by natural convection to the ambient air at temperature T_∞, by radiation exchange with the surroundings at T_{sur}, and by conduction to the aluminum plate of thermal conductivity k_{Al}.

To make the model mathematically trackable, the following assumptions were made: (1) the temperature was uniform in the sequins. (2) One-dimensional heat transfer prevailed in the aluminum plate, i.e., $\frac{\partial T_{Al}}{\partial y} = \frac{\partial T_{Al}}{\partial z} = 0$. (3) The solar radiation was collimated and normally incident on the sequin's surface. (4) Heat losses by conduction from the sequin fabric or from the aluminum plate to the polystyrene insulation was negligible. (5) The thermal paste used to attach the sequin fabric onto the aluminum plate had negligible thermal resistance so that $T_{seq}(t) = T_{Al}(x = 0,t)$. (6) Sequins were opaque and diffuse such that their spectral hemispherical emittance ε_λ was equal to the spectral hemispherical absorptance α_λ, i.e., $\varepsilon_\lambda = \alpha_\lambda$. (7) Radiation exchange between the sequin fabric and its surroundings was from a small surface to a large enclosure. (8) The ambient air and surrounding temperatures-, respectively denoted by T_∞ and T_{sur} - remained constant throughout the experiments. (9) All thermophysical properties were assumed to be constant. (10) No heat generation occurred in the system.

3.2. Governing equations

The transient energy balance for the sequins can be written as

$$C_{seq}\frac{dT_{seq}}{dt} = A\alpha_S G_S + k_{Al}A\frac{\partial T_{Al}}{\partial x}(x = 0, t) - Ah(T_{seq} - T_\infty) - A\sigma\varepsilon\left(T_{seq}^4 - T_{sur}^4\right) \quad (8)$$

where C_{seq}, α_s, and ε are the heat capacity, the solar absorptance, and the emittance of the sequin fabric of surface area A exposed to the simulated solar irradiance G_s. In addition, k_{Al} is the thermal conductivity of the aluminum plate and h is the convective heat transfer coefficient.

In order to predict the measured thermocouple temperature $T_{TC} = T_{Al}(x{=}L_{TC},t)$, the local temperature distribution at location x and time t in the aluminum plate $T_{Al}(x,t)$ was evaluated using the transient one-dimensional heat diffusion equation expressed as [8]

$$\rho_{Al}c_{p,Al}\frac{\partial T_{Al}}{\partial t} = k_{Al}\frac{\partial^2 T_{Al}}{\partial x^2} \quad (9)$$

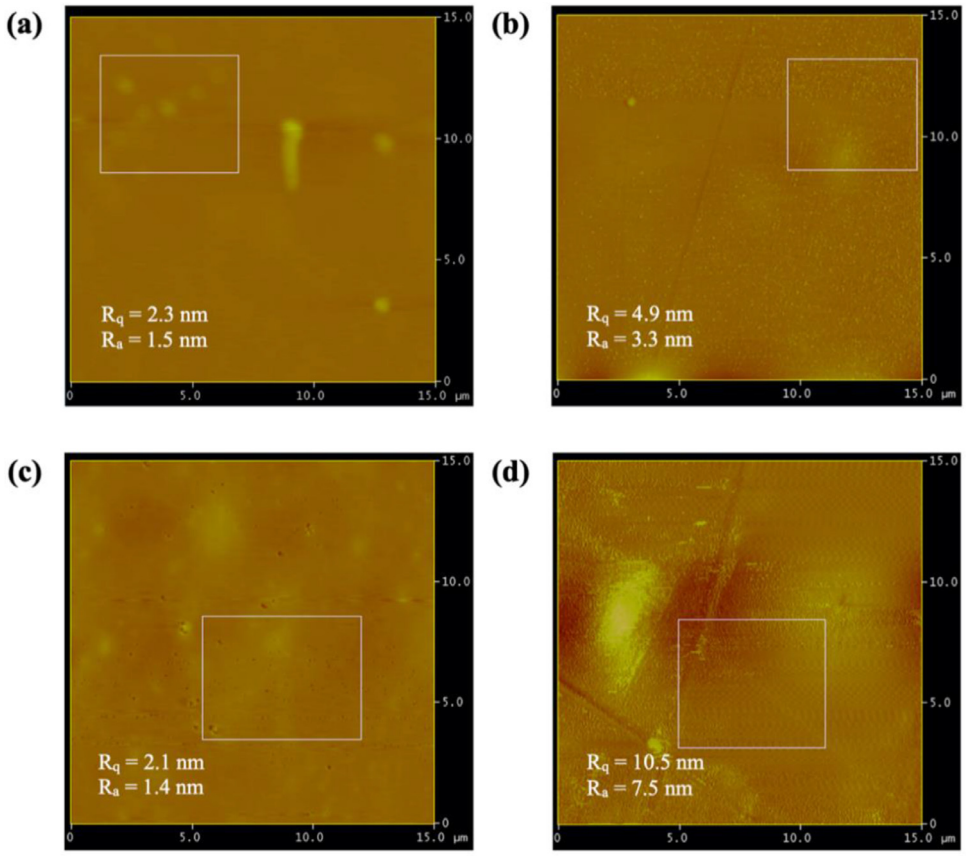

Fig. 5. AFM images for each of the sequins' (a) gold, (b) gold-black, (c) silver, and (d) silver-black side and their rms R_q and arithmetic mean R_a roughnesses.

where ρ_{Al} and $c_{p,Al}$ are the density and specific heat of aluminum, respectively. Note that at steady state, the temperature $T_{Al}(x,t)$ in the aluminum plate is uniform and the thermal model simplified to

$$\alpha_S G_S = h(T_{seq} - T_\infty) + \sigma\varepsilon\left(T_{seq}^4 - T_{sur}^4\right) \tag{10}$$

3.3. Initial and boundary conditions

In order to solve the coupled Eqs. (8) and (9) for the time-dependent temperatures $T_{seq}(t)$ and $T_{Al}(x,t)$, one needs one initial condition for $T_{seq}(t)$ and $T_{Al}(x,t)$ and two boundary conditions for $T_{Al}(x,t)$. The initial temperature of all components was assumed to be equal to the ambient air temperature T_∞, i.e.,

$$T_{seq}(t=0) = T_{Al}(x, t=0) = T_\infty = 23\ ^\circ C \tag{11}$$

The heat transfer through the polystyrene insulation was assumed to be negligible, so the temperature gradient at the back surface of the aluminum plate vanished, i.e.,

$$\frac{\partial T_{Al}}{\partial x}(x = L_{Al}, t) = 0 \tag{12}$$

The thermal resistance between the sequin fabric and the aluminum plate was assumed to be negligible. Therefore, the temperature of the aluminum plate's top surface was equal to the temperature of the sequin fabric, i.e.,

$$T_{Al}(x=0, t) = T_{seq}(t) \tag{13}$$

3.4. Closure laws

In order to solve Eqs. (8) and (9), the properties of aluminum ρ_{Al}, $c_{p,Al}$, and k_{Al} were obtained from the literature [8]. The sequin fabrics solar absorptance α_S and emissivity ε were measured experimentally while their heat capacity C_{seq} was estimated based on a weighted sum of that of the fabric and the sequins expressed as

$$C_{seq} = \left[(\rho_A c_p)_{fab} + (\rho_A c_p)_{seq}\right]A \tag{14}$$

where ρ_A is the area density (in kg/m^2) and c_p is the specific heat (in J/kg K) of the fabric or the sequins. Here, the area density ρ_A for the fabric and sequins were measured experimentally as 0.093 and 0.313 kg/m^2, respectively. The specific heats c_p of the fabric and sequins were taken, respectively as those of cotton (c_p = 1340 J/kg K) [8] and polystyrene (c_p = 1330 J/kg K) [37] to yield C_{seq} = 20.1 J/K.

In addition, the convective heat transfer coefficient h was calculated using a correlation for free convection over the upper surface of a hot flat plate valid for $10^4 < Ra < 10^7$ and $Pr \geq 0.7$ and expressed as [38]

$$\overline{Nu}_L = \frac{L_c h}{k} = C\ Ra^{0.25} \tag{15}$$

Here, the characteristic length L_c is the ratio of the sequin fabric surface area to its perimeter while C is a constant. The Rayleigh number is defined as $Ra = Pr\ Gr$ with the Prandtl and Grashof numbers defined as [8]

$$Pr = \frac{\mu c_p}{k} \text{ and } Gr = \frac{L_c{}^3 \rho^2 g \beta (T_{seq}(t) - T_\infty)}{\mu^2} \tag{16}$$

Here, ρ, μ, c_p, k, and β are the density, viscosity, specific heat, thermal conductivity, and thermal expansion coefficient of air evaluated at the mean temperature $\bar{T}(t) = (T_{seq}(t) + T_\infty)/2$ and g is the gravitational acceleration constant. Table S2 in Supplementary Materials summarizes the values of the dimensions and properties of the sequins, aluminum, and air used in solving the model.

Table 2
Summary of the mean surface roughness, solar absorptance α_s, total normal emissivity ε_n, and the ratio α_s/ε_n of the two different sequin fabrics investigated in the present study.

	Gold/black sequins		Silver/black sequins	
Property	Gold side	Black side	Silver side	Black side
Mean surface roughness, R_a (nm)	1.3 ± 0.4	7.8 ± 3.9	1.5 ± 0.3	7.1 ± 1.6
Solar absorptance α_s (0.25–3 μm)	0.39 ± 0.01	0.64 ± 0.006	0.59 ± 0.03	0.57 ± 0.02
Total normal emittance ε_n	0.13 ± 0.07	0.85 ± 0.04	0.88 ± 0.05	0.38 ± 0.04
Ratio α_s/ε_n	3	0.8	0.7	1.5

For laminar flow over a smooth flat plate ($Ra < 10^7$), the constant C has been reported as $C = 0.54$ [38]. However, the macroscopic roughness resulting from interlocking sequins renders the surface rough. Thus, the constant C was found by solving the steady-state solution of Eq. (10) using the experimental measurements for T_{seq} for the black configuration of the sequin fabric (Fig. 2). The resulting constant $C = 0.9$ was used to model free convection for both the gold and black sequin configurations.

3.5. Method of solution

The energy conservation equations expressed by Eqs. (8) and (9) were discretized using an implicit scheme of backward difference in time and central difference in space (see Supplementary Material). The discretized equations were solved numerically using Matlab.

4. Results and discussion

4.1. Material characterization

4.1.1. Surface roughness characterization

Fig. 5 shows one of the three AFM surface roughness measurements taken for each of the sequin samples for the (a) gold, (b) gold-black, (c) silver, and (d) silver-black sides. Table 2 summarizes the averages of the arithmetic mean surface roughness R_a measured at three different locations on both faces of the same sequin. It indicated that the average roughness of the colored sides (gold and silver) were both around 1.5 nm while the average roughness of the black sides on both sequin samples remained below 8 nm. Therefore, the sequin surface roughness was much smaller than the wavelengths considered. As such, the individual sequins can be assumed to be optically smooth.

4.1.2. Bulk material identification

Figure S4 shows the IR transmittance spectrum of an uncoated sequin. The first two matches for similarity in the absorption spectra was atactic polystyrene at 27% and vinylidene chloride polystyrene at 21%. These percentages are too small to confidently identify the specific plastic that makes up the substrate of the sequins but the IR absorption spectrum points to some form of polystyrene characterized by two major absorptance peaks at wavenumbers 3000 cm^{-1}, 1500 cm^{-1} and a broad band peak between 1400 and 1000 cm^{-1}. Note also that the substrate was a transparent plastic that did not dissolve in sulfuric acid, thus further pointing to some form of polystyrene.

4.1.3. Optical properties in the UV and visible range

Fig. 6 shows the spectral normal-hemispherical reflectance $\rho_{nh,\lambda}$ of the (a) gold and (b) silver sequins as a function of wavelength λ between 200 and 1100 nm. It also shows experimental uncertainty bands corresponding to two standard deviations

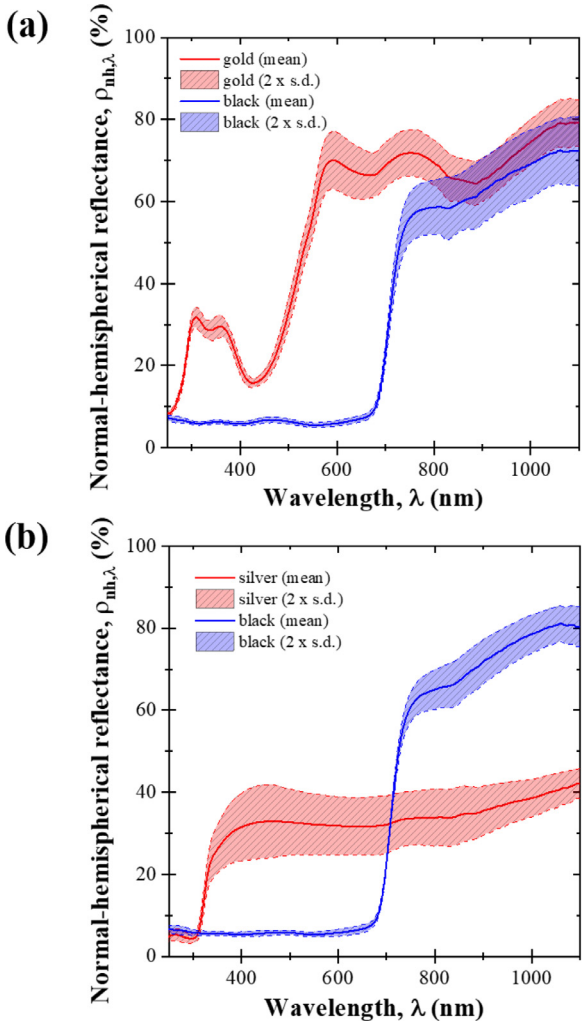

Fig. 6. Spectral-hemispherical reflectance $\rho_{h,\lambda}$ as a function of wavelength λ in the visible and NIR for (a) the gold and black sequin fabric and (b) the silver and black sequin fabric.

around the mean spectral reflectance corresponding mostly to variations in the orientation of the sequins among the measurements at six different locations of the same sample. Fig. 6 indicates that the spectral reflectance $\rho_{nh,\lambda}$ of black sides of both the gold and the silver sequins were similar and fell below 8% for wavelength between 200 and 700 nm and increased sharply to exceed 60% beyond 700 nm. On the other hand, the gold side feature larger reflectance than the black side across the spectral window of interest with a broad absorption peak around 375–450 nm. However, the reflectance of the silver side was nearly constant around 30–40% above 300 nm and fell below that of the black side for wavelength $\lambda > 700$ nm.

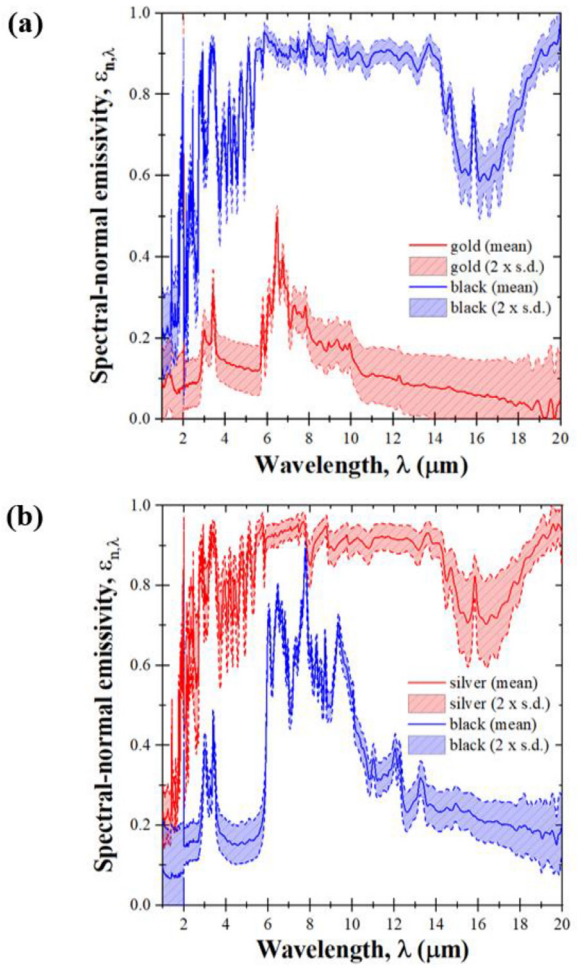

Fig. 7. Spectral normal emissivity $\varepsilon_{n,\lambda}$ as a function of wavelength λ (a) for the gold and black sequin fabric and (b) for the silver and black sequin fabric.

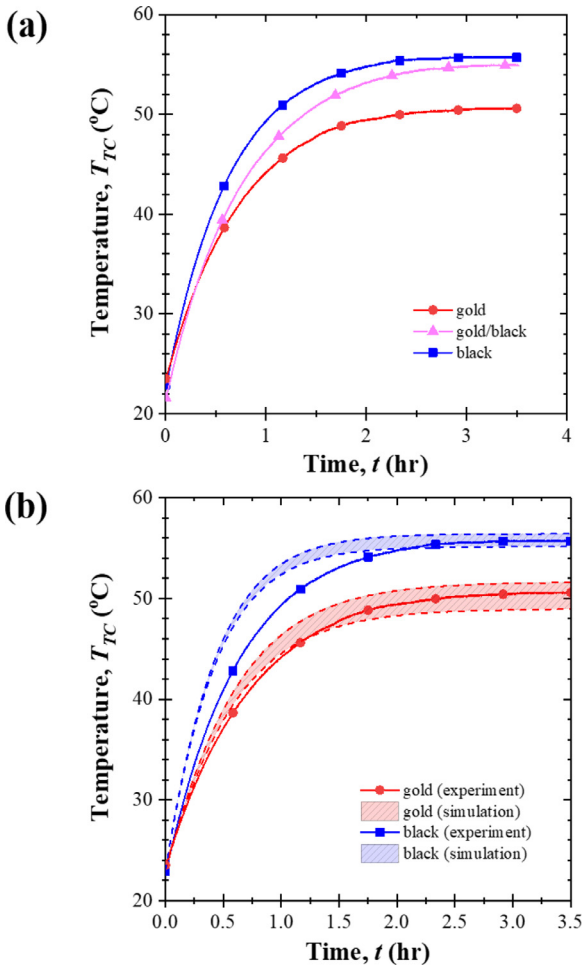

Fig. 8. (a) Experimental temperature measurements for black, 50, 50% black/gold, and gold sequin fabric. (b) Comparison between experimental and simulated temperature of the aluminum plate for all black and all gold configurations.

4.2. Spectral normal emittance $\varepsilon_{n,\lambda}$

Fig. 7 shows the spectral normal emittances $\varepsilon_{n,\lambda}$ of (a) the gold and black and (b) the silver and black sequin fabrics as functions of wavelength λ between 1 and 20 μm. Here also, the experimental uncertainty corresponds to the shaded sections while the mean value shown as the solid line. The difference in emissivity between the two sequin sides is the most pronounced for the gold and black sequin fabric. In fact, the difference in spectral normal emittance $\Delta\varepsilon_\lambda$ between the black and the gold side is greater than 0.72 in the spectral range of 4–20 μm. However, the difference in spectral normal emissivity $\varepsilon_{n,\lambda}$ between the silver and the black sides of the silver/black sequins varied between 0.88 and 0.38 across the spectral range considered due to large variations in the spectral normal emissivity of the black side.

The measured spectral normal emittance $\varepsilon_{n,\lambda}$ was used to calculate the total normal emittance ε_n and the total hemispherical emittance ε based on Eq. (6) and on the fact that $\varepsilon \approx \varepsilon_n$ [8]. Table 2 summarizes the total normal emissivity ε_n and the solar absorptance α_S of each side of the sequin along with their respective standard deviations. The gold/black sequin fabric featured a dynamic range $\Delta\varepsilon = 0.72 \pm 0.11$ at room temperature. Unexpectedly, on the other hand, the silver side had a higher emissivity than the black side. The dynamic range of the silver/black sequin fabric was $\Delta\varepsilon = 0.50 \pm 0.09$. The difference in emissivity between one face and the other can be attributed to differences in the compositions of the substrate and coating and to the thickness of the coating. Unfortunately, this information was proprietary and could not be reversed engineered. Nevertheless, the coating is expected to be a relatively simple paint and the substrate is suspected to be some form of polyester for both sequins (see Section 4.1.2). Regardless, these results demonstrate that the sequin mechanism can be used for variable emissivity surfaces. Then, the sequin fabric can be optimized for any specific application by selecting the substrate and coatings materials and thickness to achieve the desired total hemispherical emittance and/or solar absorptance to emittance ratio.

4.3. Thermal management applications

Fig. 8(a) plots the experimental temperature measurements for three configurations: black, gold, and 50, 50% black-gold. In all cases, the temperature increased rapidly from room temperature (T_∞ = 23 °C) and reached a steady-state temperature of 50.6 °C, 54.9 °C, 55.7 °C for the gold, black/gold, and black mode, respectively. The temperatures of the black/gold configuration fell between those of the black and gold configurations. This demonstrates the ability to tune the system's temperature by adjusting the pattern of the sequins.

Moreover, the gold side had a larger solar absorptance to emissivity ratio α_s/ε than the black side. Thus, in absence of convection, the steady-state temperature of the gold sequins would reach 476 K and exceed that of the black sequins estimated at 339 K,

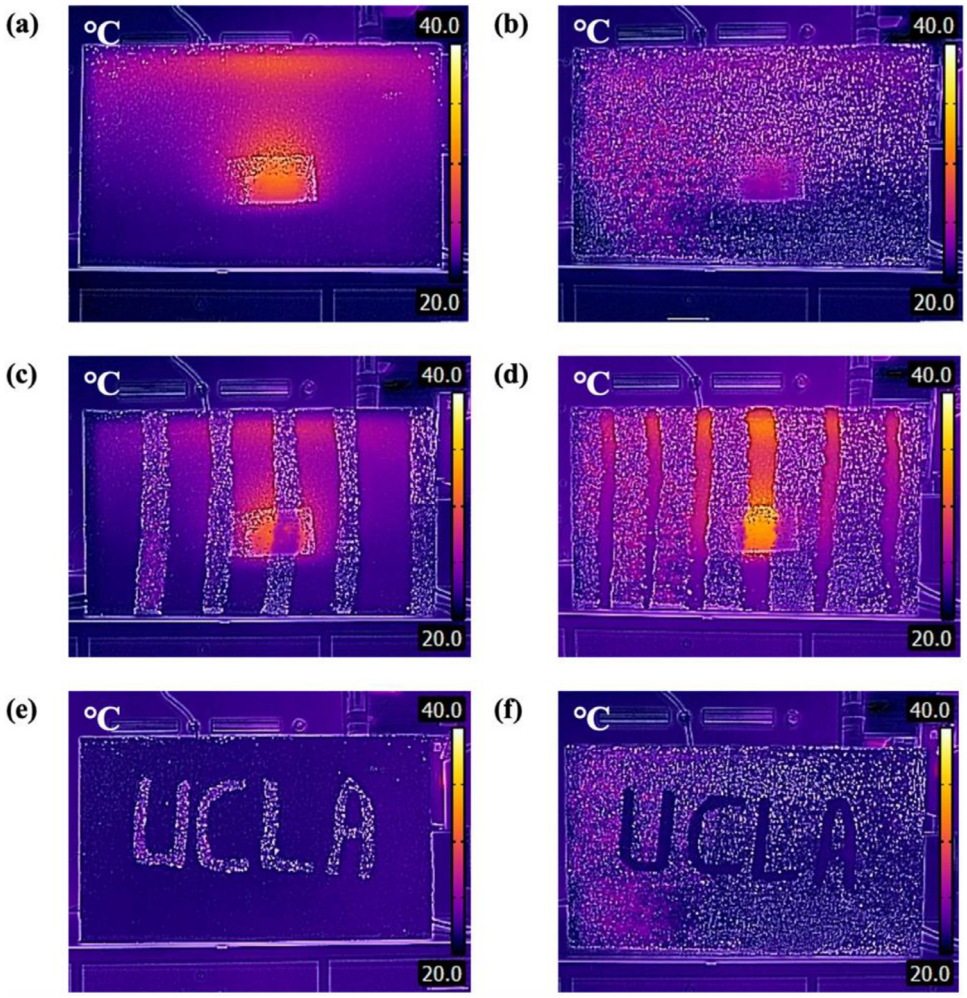

Fig. 9. IR images with temperature scale in °C illustrating the use of sequin fabric (a,b) for thermal camouflage with sequin fabric in black and gold mode (lamp on). (c,d) for thermal illusion with sequins in black mode with gold stripes and gold mode with black stripes (lamp on). (e,f) thermal messaging reading "UCLA" written in gold on black or and black on gold (light off).

per Eq. (2). However, experimentally, the sequins were also subjected to convective heat transfer which dominated over thermal radiation emissions. Therefore, the steady-state temperature of the black sequins was larger than that of the gold sequins because of their larger solar absorptance α_s as $T_{seq}(t \to \infty) \approx T_\infty + \alpha_S G_S/h$.

4.4. Thermal model

Fig. 8(b) compares the measured and simulated temporal evolution of the Al plate temperature for the gold and black surfaces. The initial temperature for both configurations was taken as 23 °C. The shaded area between the two dotted lines represents the upper and lower limits of the temperature predictions for each sequin side and corresponds to a range of possible temperatures. This interval was determined using the uncertainty associated with the emissivity and absorptance measurements (Table 2). Overall, the experimental measurements fell within the prediction range under the combined effect of natural convection and radiation exchanges between the simulated solar radiation and the gold or black sequin surfaces.

4.5. Camouflage applications

Fig. 9 shows infrared images (temperature scale in °C) of the experimental setup of Fig. 3 featuring an incandescent lightbulb behind the gold/black sequin fabric to illustrate the uses of the sequins for thermal camouflage, illusion, and messaging. First, the sequin fabrics investigated are bendable, cheap, and scalable to any small or large surface. The sequins are also durable and compatible with large scale roll to roll manufacturing. Second, Fig. 9(a,b) shows the thermal camouflage capability of the sequin fabric. Although the temperature map of the fabric was the same in both IR images, the thermal signature of the heat source is clearly identifiable in Fig. 9(a) when the black side of the sequin is used. However, the heat source cannot be seen in Fig. 9(b) as the fabric temperature appears uniform after flipping the sequins from black to gold in the region covering the lamp, thanks to the previously documented changes in emissivity between the black and gold sides of the sequins.

Furthermore, unique patterns or images may be created by flipping only particular sequins to the high-emissivity side, creating an illusion by fooling a thermal imager into misidentifying the cloaked object. Fig. 9(c,d) demonstrates such thermal illusion by using stripes on the sequin fabric, as illustrated in Fig. 3(c). Such pattern gave the illusion of the presence of a fence in front of the heat source and/or the impression that the heat source was smaller or had a different shape than the reality.

Finally, thermal messaging follows from the idea that patterns or words can be created on the sequin fabric, as highlighted in Fig. 9(e,f) with the message "UCLA" written in the IR image. Al-

though the results may not represent the final, optimized, battle-ready form of camouflage, it is important to note that these sequins were procured off-the-shelf, and were not initially intended for thermal applications. Therefore, these preliminary results provide an illustration of sequin fabrics potential applications for thermal camouflage, illusion, messaging. Further optimization of the sequin shape, materials, coating, and connection to the underlying fabric could address these challenges.

5. Conclusion

This proof of concept study demonstrated that reversible sequin fabrics can be used as an effective variable emittance surface. The emissivity dynamic range at room temperature was measured as 0.72 ± 0.11 between the two sides of the sequins of a commercial gold and black colored sequin fabric. In addition, the solar absorption to emissivity ratio ranged from 0.8 to 3. Moreover, exposing the fabric to simulated solar radiation for different configurations of the sequins resulted in large differences in the systems temperatures thanks to the change in emissivity and solar absorptance. A first order thermal model was able to predict the experimental data. The sequins were also shown to be effective surface for thermally camouflage, through infrared imagery. Finally, the radiation performance of the fabric can be further optimized for a specific application by carefully choosing the coatings and substrate of the sequins. Similarly, an actuation method should be developed for specific applications.

Declaration of Competing Interest

The authors have no competing interest to declare.

CRediT authorship contribution statement

Frank Huisman: Conceptualization, Methodology, Validation, Formal analysis, Data curation, Visualization, Writing – original draft. **Eylul Simsek:** Validation, Investigation, Writing – review & editing. **Tiphaine Galy:** Conceptualization, Methodology, Validation, Formal analysis, Investigation, Writing – review & editing. **Fadi Samaan:** Software, Formal analysis, Data curation, Visualization, Writing – original draft. **Laurent Pilon:** Conceptualization, Methodology, Resources, Project administration, Supervision, Writing – review & editing.

Acknowledgment

The authors would like to thank Zihao Qin for his help with the AFM images and measurements of the sequin samples, Dr. Michal Marszewski for his help in sample preparation for substrate identification, Gabriel Fernandez and Nicole Durghalli for their help with the IR camera pictures. Finally, LP is grateful to his daughter EHP for the inspiration and for introducing him to the beauty of sequin fabrics.

Supplementary materials

Supplementary material associated with this article can be found, in the online version, at doi:10.1016/j.ijheatmasstransfer.2021.122167.

References

[1] D. Gilmore, Spacecraft Thermal Control Handbook: Fundamental Technologies Vol 2, American Institute of Aeronautics & Astronautics, Washington DC, 2002.
[2] N. Athanasopoulos, J. Siakavellas, “Variable emissivity through multilayer patterned surfaces for passive thermal control: preliminary thermal design of a nano-satellite”, in: Proceedings of the 48th International Conference on Environmental Systems, Albuquerque, United States, 2018 July 8-12.
[3] J. Gong, G. Cha, Y.S. Ju, C. Kim, "Thermal switches based on coplanar EWOD for satellite thermal control", in: Proceedings of the IEEE International Conference on Micro Electro Mechanical Systems (MEMS), Tucson, AZ United States, 2008 January 13–17.
[4] O. Thorén, "BAE systems international", 2020, [Online]. Available: www.baesystems.com/en/feature/adativ-cloak-of-invisibility. [Accessed 9 August 2020].
[5] P. Chandrasekhar, B. Zay, D. Lawrence, E. Caldwell, R. Sheth, R. Stephan, J. Cornwell, "Variable-emittance infrared electrochromic skins combining unique conducting polymers, ionic liquid electrolytes, microporous polymer membranes, and semiconductor/polymer coatings, for spacecraft thermal control", J. Appl. Polym. Sci. 131 (19) (2014) 40850.
[6] H. Ji, D. Liu, H. Cheng, C. Zhang, L. Yang, "Vanadium dioxide nanopowders with tunable emissivity for adaptive infrared camouflage in both thermal atmospheric windows", Sol. Energy Mater. Sol. Cells 175 (2018) 96–101.
[7] C. Massina, D. Klaus, "Prospects for implementing variable emittance thermal control of space suits on the martian surface", J. Therm. Sci. Eng. Appl. 8 (4) (2016) 041002.
[8] T.L. Bergman, A.S. Lavine, Fundamentals of Heat and Mass Transfer, 8th ed., John Wiley & Sons, Hoboken, NJ, 2017.
[9] J. Wertz, D. Everett, J. Peschell, Space Mission Engineering: The New SMAD, Microcosm Press, Hawthorne, CA, 2011.
[10] Sierra Nevada Coropration, "Space technologies product catalogue", 2018. [Online]. Available: https://www.sncorp.com/media/2544/spt-catalog-master_2018_reduced.pdf
[11] D. Farrar, W. Schneider, R. Osiander, J. Champion, A. Damn, "Controlling variable emittance (MEMS) coatings for space applications", in: Proceedings of the Intersociety Conference on Thermal Phenomena, San Diego, CA United States, 2002 May 29–June 1.
[12] D. Ren, J. Tian, "Modeling and analysis of a MEMS-based thermal emissivity variable thermal control device", Appl. Mech. Mater. 401-403 (2013) 1686–1690.
[13] S. Cao, X. Chen, G. Wu, J. Yang, R. Wang, K. Shang, L. Wang, "Variable emissivity surfaces for micro and nano-satellites", Phys. Procedia 18 (2011) 91–94.
[14] E. Sparrow, S. Lin, "Absorption of thermal radiation in a V-groove cavity", Int. J. Heat Mass Transf. 5 (11) (1962) 1111–1115.
[15] R.B. Mulford, M.R. Jones, B.D. Iverson, "Dynamic control of radiative surface properties with origami-inspired design", ASME J. Heat Transf. 138 (3) (2016) 032701.
[16] R.B. Mulford, V.H. Dwivedi, M.R. Jones, B.D. Iverson, “Control of net radiative heat transfer with a variable-emissivity accordion tessellation”, ASME J. Heat Transf. 141 (3) (2019) 032702.
[17] R.B. Mulford, N.S. Collins, M.S. Farnsworth, M.R. Jones, B.D. Iverson, “Total hemispherical apparent radiative properties of the infinite V-groove with diffuse reflection”, AIAA J. Thermophys. Heat Transf. 32 (4) (2018) 1108–1112.
[18] R.B. Mulford, N.S. Collins, M.S. Farnsworth, M.R. Jones, B.D. Iverson, “Total hemispherical apparent radiative properties of the infinite V-groove with specular reflection”, Int. J. Heat Mass Transf. 124 (2018) 168–176.
[19] R. Hu, Y. Liu, S. Shin, S. Huang, X. Ren, W. Shu, J. Cheng, G. Tao, W. Xu, R. Chen, X. Luo, “Emerging materials and strategies for personal thermal management”, Adv. Energy Mater. 10 (17) (2020) 921–944.
[20] F. Lang, H. Wang, S. Zhang, J. Liu, H. Yan, "Review on variable emissivity materials and devices based on smart chromism", Int. J. Thermophys. 39 (2018) 6.
[21] H. Demiryont, D. Moorehead, "Electrochromic emissivity modulator for spacecraft thermal management", Sol. Energy Mater. Sol. Cells 93 (2009) 2075.
[22] L. Zhao, R. Zhang, C. Deng, Y. Peng, T. Jiang, "Tunable infrared emissivity in multilayer graphene by ionic liquid intercalation", Nanomaterials 9 (8) (2019) 1096.
[23] O. Salihoglu, H. Uzlu, O. Yakar, S. Aas, O. Balci, N. Kakenov, S. Balci, S. Olcum, S. Süzer, C. Kocabas, "Graphene-based adaptive thermal camouflage", Nano Lett. 18 (7) (2018) 4541–4548.
[24] S. Wu, C. Jia, X. Fu, X. Weng, J. Zhang, L. Deng, "A novel electrochromic and broad infrared emissivity modulation film based on the copolymer of aniline and o-anisidine", Electrochim. Acta 88 (2013) 322–329.
[25] I. Schwendeman, J. Hwang, D. Welsh, D. Tanner, J. Reynolds, "Combined visible and infrared electrochromism using dual polymer devices", Adv. Mater. 13 (9) (2001) 634–637.
[26] S. Tachikawa, A. Ohnishi, Y. Shimakawa, A. Ochi, A. Okamoto, Y. Nakamura, "Development of a variable emittance radiator based on a perovskite manganese oxide", J. Thermophys. Heat Transf. 17 (2) (2003) 264–268.
[27] D. Fan, Q. Li, Y. Xuan, H. Tan, "Degradation of thermal radiative properties of variable emissivity device based on manganese oxides in simulated space environment", Int. J. Therm. Sci. 71 (2013) 258–263.
[28] R. Voti, M. Larciprete, G. Leahu, C. Sibilia, M. Bertolotti, "Optimization of thermochromic VO_2 based structures with tunable thermal emissivity", J. Appl. Phys. 112 (2012) 23–33.
[29] A. Hendaoui, N. Émond, M. Chaker, É. Haddad, “Highly tunable-emittance radiator based on semiconductor-metal transition of VO_2 thin films”, Appl. Phys. Lett. 102 (6) (2013) 061107.
[30] D. Liu, X.Xing H.Cheng, C. Zhang, W. Zheng, "Thermochromic properties of W–doped VO_2 thin films deposited by aqueous sol-gel method for adaptive infrared stealth application", Infrared Phys. Technol. 77 (2016) 339–343.
[31] R. Hu, W. Xi, Y. Liu, K. Tang, J. Song, X. Luo, J. Wu, C.W Qiu, “Thermal camouflaging metamaterials”, Mater. Today 45 (2021) 120–141.

[32] R. Hu, S. Zhou, Y. Li, D.Y. Lei, X. Luo, C.W. Qiu, “Illusion thermotics”, Adv. Mater. 30 (2018) 237–245.
[33] J. Song, S. Huang, Y. Ma, Q. Cheng, R. Hu, X. Luo, “Radiative metasurface for thermal camouflage, illusion and messaging”, Opt. Express 28 (2) (2020) 875–885.
[34] Y. Liu, J. Song, W. Zhao, X. Ren, Q. Cheng, X. Luo, N.X. Fang, R. Hu, “Dynamic thermal camouflage via a liquid-crystal- based radiative metasurface”, Nanophotonics 9 (4) (2020) 855–863.
[35] C. Cooksey, D. Allen, B. Tsai, "Reference data set of human skin", J. Res. Natl. Inst. Stand. Technol. 122 (2017) 1–5.
[36] ASTM International, Designation: E408 –13"Standard Test Methods For Total Normal Emittance of Surfaces Using Inspection-Meter Techniques", ASTM International, West Conshohocken, PA, 2019.
[37] B.S. Hemingway, R.A. Robie, "Heat Capacity of Polystyrene From 275 to 315 K", U.S. Geological Survey, 1994 Report 94-671.
[38] R. Goldstein, E. Sparrow, D. Jones, "Natural convection mass transfer adjacent to horizontal plates", Int. J. Heat Mass Transf. 16 (1973) 1025–1035.